JOURNAL of
MATERIALS and MECHATRONICS:A

e-ISSN 2717-8811
JournalMM, 2023, 4(1), 224-243
https://doi.org/10.55546/jmm.1261024

Araştırma Makalesi / Research Article

Thermomechanical Response of Functionally Graded Ti-6Al-4V and Zirconia Biomaterial Plates

Ramazan ÖZMEN

Karabük University, Engineering Faculty, Mechatronics Engineering Department, Karabük, Türkiye,
ORCID ID: https://orcid.org/0000-0002-6020-8538, ramazanozmen@karabuk.edu.tr

Geliş/ Received: 06.03.2023; **Kabul / Accepted:** 04.04.2023

ABSTRACT: This article studies the free vibration and thermal buckling responses of functionally graded material (FGM) porous nanoplates exposed to thermal load. The developed mathematical model includes a shear deformation, size-scale, and microstructure influence by a high-order shear deformation and nonlocal strain gradient theories. The study considers four different porosity patterns across the thickness: uniform, symmetrical, asymmetric bottom, and asymmetric top distributions. The equation of motion of the FGM porous nanoplate, including the effects of thermal load, was derived with Hamilton's principle, and then solved analytically by employing the Navier method. Especially the temperature-dependent material properties of Ti-6Al-4V and Zirconia are involved in the model in calculating thermal loads due to their effectiveness in the dynamic behavior of the nanoplate. For the free vibration responses of the nanoplate, the effects of nonlocal and strain gradient elasticities, temperature rise, porosity volume fraction and its distribution have been analyzed. The results reveal significant influences of porosity and its distribution pattern, material's volumetric dispersion, size dependency, and temperature on the plate's free vibration and buckling temperatures.

Keywords: Porosity, Functionally Graded Material, Nanoplate, Nonlocal strain gradient theory, Thermal load.

*Sorumlu yazar / Corresponding author: ramazanozmen@karabuk.edu.tr

Bu makaleye atıf yapmak için /To cite this article

Özmen, R. (2023). Thermomechanical Response of Functionally Graded Ti-6Al-4V and Zirconia Biomaterial Plates. Journal of Materials and Mechatronics: A (JournalMM), 4(1), 224-243.

1. INTRODUCTION

Many diverse types of engineering structures frequently employ laminated composite materials. In common laminated composite constructions, homogeneous elastic laminae are linked together to produce improved mechanical characteristics. However, significant interlaminar stresses, causing delamination, can be induced by sudden material characteristic changes at the interface between two materials (Zenkour, 2005). Functionally graded materials (FGMs), usually consisting of ceramic and metal mixtures, are developed to overcome the drawbacks of classical composites by providing a smooth material transition. In these materials, the interface problems of classical composites can be eliminated by gradually changing the volume fraction of the constituent materials in the thickness direction. Thus, a smooth stress distribution is provided (Zenkour and Alghamdi, 2010). The powder metallurgy method is the most suitable and applicable process for FGM production. Porosity, controlled by compression and sintering temperature and time, is one of the critical parameters affecting the mechanical behavior of the parts produced with powder metallurgy (Pasha and B.M., 2022; Şanlı and Gavas, 2021).

Because of its excellent mechanical, biocompatibility, and corrosion resistance, titanium and its alloys are frequently employed in biomedical equipment. Ti-6Al-4V is one of the most popular titanium alloys due to its excellent mechanical and physical properties. In addition, ZrO_2 is a medical ceramic frequently used in dental applications, and its benefits, including strong biocompatibility, simple sterilization, and shaping, have drawn increasing attention (X. Zhang et al. 2018, Zhou et al. 2022). Also, it can be used as a second phase to reduce the sintering temperature and improve the mechanical properties of boron carbide (Biçer 2022). Besides using Ti-6Al-4V/ZrO_2 in biomedical applications, Ti-6Al-4V has been commonly utilized in the automotive industry, medical instruments, and gas turbines, due to its superior performance, such as high fracture toughness, specific strength, and corrosion resistance. Meanwhile, as a thermal barrier, zirconia is frequently bonded with Ti-6Al-4V to manufacture some complex parts used in aircraft turbines. Therefore, joining Ti-6Al-4V and ZrO_2 properly are crucial to achieve excellent joints (C. Zhang et al., 2020).

Recently, a substantial investigation has been performed on the dynamic behavior of small-scale structures under thermal and mechanical loads. However, the classical theories need to be revised to predict the dynamic behavior of micro/nanoscale structures. For this reason, to consider the small-scale effects, various theories have been proposed so far, such as the micro-morphic theory (MMT) defined by (Eringen and Suhubi, 1964), the nonlocal elasticity theory (NET) (Eringen, 1983), the strain gradient elasticity theory (SGT) (Kong et al., 2008), the modified couple stress theory (MCST) (Ke et al., 2012) and the nonlocal strain gradient theory (NSGT) (Li and Hu, 2015).

Porous small-scale structures under several loads and environments are gaining significance nowadays, and the free vibration and bending response of functionally graded material (FGM) porous nanoplates have been studied in numerous studies. Barati and Zenkour examined an FGM nanoplate's post-buckling behavior, considering the geometric imperfections and porosity based on the NET and high-order shear deformation theory (HSDT) (Barati and Zenkour, 2019). Bendaho et al. studied an FGM nanoplate's free vibration analysis using the 2D and quasi-3D nonlocal shear deformation theories (Bendaho et al., 2019). By combining the finite element method (FEM) and nonlocal theory, Doan et al. analyzed the free vibration response of FGM porous nanoplates with different shapes, considering foundation effects (Doan et al., 2021). Kiani examined a carbon nanotube (CNT) reinforced composite plate's post-buckling problem subjected to uniform temperature rise using first-

order shear deformation theory (FSDT) (Kiani, 2017). The study, examining the effect of uniform or functionally grading distribution of the CNTs used as reinforcement, stated that the X-type FGM distribution of the CNT model resulted in higher buckling temperature and reduced the plate's deflection after buckling. Talebizadehsardari et al. developed a closed-form solution based on the third-order shell theory (TSDT) for the free vibration of porous FGM micro-nano shells (Talebizadehsardari et al., 2020). Using the TSDT, Coskun et al. examined an FGM porous microplate's static bending, free vibration, and buckling behavior (Coskun et al., 2019). They stated that every porosity distribution's effect is discerned due to the connection among the porosity variation and the material properties' heterogeneity.

The studies on FGM porous nanoplates are limited in the literature and have only addressed the free response of porous nanoplates with uniform and random porosity distributions. This study aims to investigate the free vibration and buckling response of an FGM porous nanoplate exposed to a thermal load using the HSDT and NGST. The nanoplate consists of Zirconia (ZrO_2) and Titanium (Ti-6Al-4V) constituents that are graded according to a power law across the thickness. The porosity is inevitable due to the nature of such structures. In addition, it may be desirable to create porosity for lightweight structures by design in specific areas of use. The proposed method considers four different porosity distributions and models for FGM porous nanoplates using the HSDT and NGST. Especially the temperature-dependent material properties of the plate's constituents, Zirconia (ZrO_2) and Titanium (Ti-6Al-4V), are considered in the study due to their effectiveness in the dynamic behavior of the nanoplate. By applying Navier's method, the effects of porosity distribution, nonlocal and size parameters, and thermal force are analyzed, and some interesting new results are also presented.

2. MATERIALS AND METHODS

Figure 1 depicts a porous FGM nanoscale plate in a thermal environment with the sizes *a* (width), *b* (length), and *h* (thickness). In contrast, the nanoplate's upper and lower surfaces are, in turn, made of Zirconia (ZrO_2) and Titanium (Ti-6Al-4V). Moreover, these two components are functionally graded according to a power law between surfaces. The temperature-dependent material properties and porosity distribution patterns are explained below.

2.1 Temperature-dependent material properties

The effective material properties of ceramic (ZrO_2) and metal (Ti-6Al-4V) material constituents can be defined as temperature-dependent with the following (Touloukian 1967; Esen, 2021a; Esen, 2021b):

$$P = P_0(P_{-1}T^{-1} + 1 + P_1T + P_2T^2 + P_3T^3) \quad (1)$$

As presented in Table 1, the symbols of P_0, P_{-1}, P_1, P_2, and P_3 are experimentally defined characteristic material constants based on degrees of temperature T. Because of the nano-size, a uniform temperature rise case is only managed with a stress-free state at (T_0 = 300 K), where $\Delta T = T - T_0$.

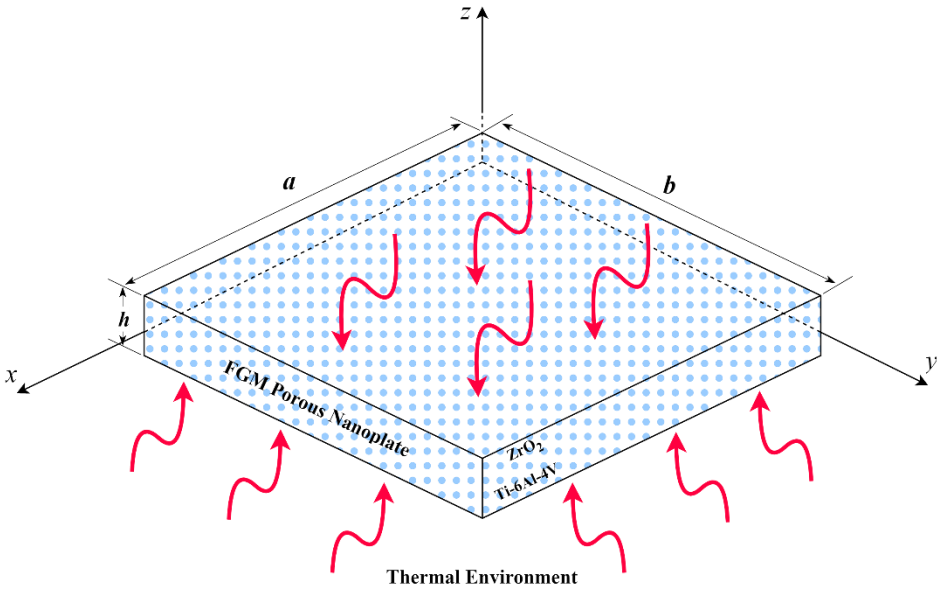

Figure 1. An FGM porous nanoplate in a thermal field

2.2 Porosity patterns and effective properties

The plate's effective material properties can be defined by the volume fractions (V_c and V_m) and properties (P_c and P_m) of ceramic and metal components, according to a power-law grading with the following formula (Najafi et al., 2017; Esen 2019):

$$P_{ef} = V_c P_c + V_m P_m$$
$$V_c = \left(\frac{z}{h} + \frac{1}{2}\right)^p , V_m = 1 - V_c \qquad 0 \le n < \infty \tag{2}$$

where p is the material grading (power-law) constant. According to Equation (2), the density, modulus of elasticity, Poisson's ratio, and thermal expansion coefficient of an FGM plate without porosity are obtained as follows. (Reddy and Chin, 1998):

$$P(z) = [P_c - P_m]V_c + P_m \tag{3}$$

In this study, four types of porosity distribution across the thickness are considered as given in Figure 2. Accordingly, the effective material properties are obtained by substituting the total volume fraction (α) of porosity in Equation (2). Thus, by using Equation (2), Equations (4-7) are obtained for uniform, symmetric, asymmetric top and asymmetric bottom porosity patterns, respectively (Esen et al., 2022; Esen and Özmen 2022a).

$$P(z) = [P_c - P_m]V_c + P_m - \frac{\alpha}{2}[P_c + P_m] \tag{4}$$

$$P(z) = \{[P_c - P_m]V_c + P_m\}\left\{1 - \alpha \cos\left[\pi \frac{z}{h}\right]\right\} \tag{5}$$

$$P(z) = \{[P_c - P_m]V_c + P_m\}\left\{1 - \alpha\, cos\left[\frac{\pi}{2}\left(\frac{z}{h} + \frac{1}{2}\right)\right]\right\} \tag{6}$$

$$P(z) = \{[P_c - P_m]V_c + P_m\}\left\{1 - \alpha\, cos\left[\frac{\pi}{2}\left(\frac{z}{h} - \frac{1}{2}\right)\right]\right\} \tag{7}$$

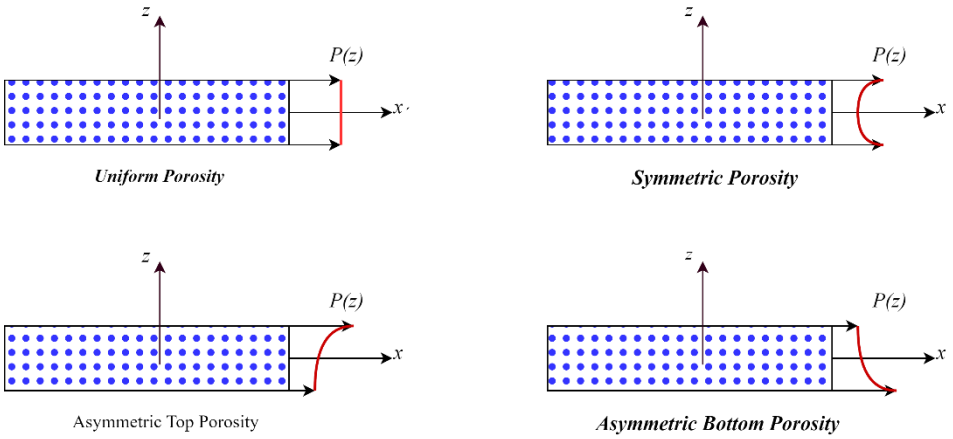

Figure 2. Porosity distribution patterns across the thickness

2.3 Constitutive Relations

Using the HSDT, the displacement field is in the form (Aghababaei and Reddy 2009; Akavci, 2014)

$$\begin{aligned} u(x,y,z,t) &= u_0(x,y,t) - zw_{0,x} + f(z)\phi_x(x,y,t) \\ v(x,y,z,t) &= v_0(x,y,t) - zw_{0,y} + f(z)\phi_y(x,y,t) \\ w(x,y,z,t) &= w_0(x,y,t) \end{aligned} \tag{8}$$

Here, u, v, and w are the displacements and $u_0(x,y,t)$ $v_0(x,y,t)$ and $w(x,y,t)$ represent the mid-plane displacements, and $\phi_x(x,y,t)$ and $\phi_y(x,y,t)$ are the cross-section's rotations, and $(.)_{,x}$ and $(.)_{,y}$ imply the partial derivatives for x and y. Finally, the parabolic shape function $f(z)$ is assumed as (Reddy 1984; Aghababaei and Reddy, 2009):

$$f(z) = z - \frac{H_t}{\pi} sin\,(\frac{\pi z}{H_t}) \tag{9}$$

$$\begin{Bmatrix} \varepsilon_{xx} \\ \varepsilon_{yy} \\ \gamma_{xy} \\ \gamma_{yz} \\ \gamma_{xz} \end{Bmatrix} = \begin{Bmatrix} u_{0,x} - zw_{0,xx} + f(z)\phi_{xx} \\ v_{0,y} - zw_{0,yy} + f(z)\phi_{yy} \\ u_{0,y} + v_{0,x} - 2zw_{0,xy} + f(z)(\phi_{x,y} + \phi_{y,x}) \\ \acute{f}(z)\phi_y \\ \acute{f}(z)\phi_x \end{Bmatrix} \tag{10}$$

Here,

$$g(z) = 1 - \frac{df(z)}{dz} \tag{11}$$

Including the thermal effect, the constitutive relationships of the HSDT and NSGT for the porous FGM nanoplate can be stated as follows (Lim et al., 2015; Jalaei and Thai 2019):

$$\begin{Bmatrix}\sigma_{xx}\\ \sigma_{yy}\\ \tau_{xy}\\ \tau_{yz}\\ \tau_{xz}\end{Bmatrix}\left[1-(ea)^2\nabla^2\right]=\begin{bmatrix}Q_{11} & Q_{12} & 0 & 0 & 0\\ Q_{12} & Q_{22} & 0 & 0 & 0\\ 0 & 0 & Q_{66} & 0 & 0\\ 0 & 0 & 0 & Q_{44} & 0\\ 0 & 0 & 0 & 0 & Q_{55}\end{bmatrix}\begin{Bmatrix}\varepsilon_{xx}-\alpha_{xx}\Delta T\\ \varepsilon_{yy}-\alpha_{yy}\Delta T\\ \gamma_{xy}\\ \gamma_{yz}\\ \gamma_{xz}\end{Bmatrix}[1-l_m^2\nabla^2] \tag{12}$$

where ε and γ are the normal and shear strains, and the stiffnesses Q_{ij} are:

$$Q_{11}=Q_{22}=\frac{E(z)}{1-v^2},Q_{12}=\frac{vE(z)}{1-v^2},\quad Q_{44}=Q_{55}=Q_{66}=\frac{E(z)}{2(1+v)} \tag{13}$$

And the resultants of the force and moment can be defined as;

$$\begin{Bmatrix}N\\ M\\ P\end{Bmatrix}=\begin{bmatrix}A_{ij} & B_{ij} & C_{ij}\\ B_{ij} & D_{ij} & E_{ij}\\ C_{ij} & E_{ij} & G_{ij}\end{bmatrix}\begin{Bmatrix}\varepsilon\\ \kappa\\ \kappa_\phi\end{Bmatrix},(i,j=1,2,6) \tag{14}$$

$$\{R\}=\left[F_{ij}\right]\{\phi\},(i,j=4,5) \tag{15}$$

where,

$$\begin{gathered}N=\begin{Bmatrix}N_x\\ N_y\\ N_{xy}\end{Bmatrix},\qquad M=\begin{Bmatrix}M_x\\ M_y\\ M_{xy}\end{Bmatrix},\qquad P=\begin{Bmatrix}P_x\\ P_y\\ P_{xy}\end{Bmatrix},\qquad R=\begin{Bmatrix}R_x\\ R_y\end{Bmatrix},\\ \varepsilon=\begin{Bmatrix}u_{0,x}\\ v_{0,y}\\ u_{0,y}+v_{0,x}\end{Bmatrix},\qquad \kappa=\begin{Bmatrix}w_{0,xx}\\ w_{0,yy}\\ 2w_{0,xy}\end{Bmatrix},\qquad \kappa_\phi=\begin{Bmatrix}\phi_{x,x}\\ \phi_{y,y}\\ \phi_{x,y}+\phi_{y,x}\end{Bmatrix},\qquad \phi=\begin{Bmatrix}\phi_x\\ \phi_y\end{Bmatrix}\end{gathered} \tag{16}$$

and the stiffness coefficients are described by:

$$\begin{gathered}(A_{ij},B_{ij},C_{ij},D_{ij},E_{ij},G_{ij})=\int_{-h/2}^{h/2}(1,z,f(z),z^2,zf(z),f(z)^2)Q_{ij}dz\qquad(i,j=1,2,6),\\ F_{ij}=\int_{-h/2}^{h/2}(g(z))^2Q_{ij}dz\quad i,j=4,5\end{gathered} \tag{17}$$

Thermally-induced force and moment are described by (Kiani, 2017):

$$\begin{bmatrix}N_{xx}^T & M_{xx}^T\\ N_{yy}^T & M_{yy}^T\end{bmatrix}=\int_{-h/2}^{h/2}\begin{bmatrix}Q_{11} & Q_{12}\\ Q_{12} & Q_{22}\end{bmatrix}\begin{bmatrix}\alpha_{xx}(z,T)\\ \alpha_{yy}(z,T)\end{bmatrix}\Delta T(1,z)dz \tag{18}$$

Strain energy

$$U=\frac{1}{2}\int_V(\sigma_{xx}\varepsilon_{xx}+\sigma_{yy}\varepsilon_{yy}+\tau_{xy}\gamma_{xy}+\tau_{xz}\gamma_{xz}+\tau_{yz}\gamma_{yz})dV \tag{19}$$

Kinetic energy

$$T = \frac{1}{2}\int_0^a \int_0^b \int_{-h/2}^{h/2} \rho(z)[(\dot{u}^2 + \dot{v}^2 + \dot{w}^2)]\, dzdydx \tag{20}$$

The external potential energy of transverse $q(x, y, t)$ and thermal loads

$$V_{qT} = \int_\Omega \left[q(x, y, t)w_0 - N_{xx}^T \frac{\partial^2 w_0}{\partial x^2} - N_{yy}^T \frac{\partial^2 w_0}{\partial y^2} \right] d\Omega \tag{21}$$

Using the Hamilton principle (Reddy, 2007)

$$\int_{t1}^{t2} (\delta T - \delta U + \delta(V_{qT})dt = 0 \tag{22}$$

By substituting Equations (19), (20) and (21) into Equation (22) and after performing the integration, setting each coefficient of $\delta u_0, \delta v_0, \delta w_0, \delta \phi_x$ and $\delta \phi_y$ to zero, the equations of motion are:

$$\left(1 - l_m^2 \frac{\partial^2}{\partial x^2}\right) \begin{bmatrix} N_{x,x} + N_{xy,y} \\ N_{xy,x} + N_{y,y} \\ M_{x,xx} + M_{y,yy} + 2M_{xy,xy} \\ P_{x,x} + P_{xy,y} - R_x \\ P_{xy,x} + P_{y,y} - R_y \end{bmatrix} = \left(1 - (ea)^2 \frac{\partial^2}{\partial x^2}\right) \begin{bmatrix} I_1\ddot{u}_0 - I_2\ddot{w}_{0,x} + I_4\ddot{\phi}_x \\ I_1\ddot{v}_0 - I_2\ddot{w}_{0,y} + I_4\ddot{\phi}_y \\ S + \Psi \\ I_4\ddot{u}_0 - I_5\ddot{w}_{0,x} + I_6\ddot{\phi}_x \\ I_4\ddot{v}_0 - I_5\ddot{w}_{0,y} + I_6\ddot{\phi}_y \end{bmatrix} \tag{23}$$

With,

$$\begin{gathered} S = I_1\ddot{w}_0 + I_2\left(\ddot{u}_{0,x} + \ddot{v}_{0,y}\right) - I_3\left(\ddot{w}_{0,xx} + \ddot{w}_{0,yy}\right) - I_5\left(\ddot{\phi}_{x,x} + \ddot{\phi}_{y,y}\right) \\ \Psi = -q - N_{xx}^T w_{0,xx} + N_{yy}^T w_{0,yy} \end{gathered} \tag{24}$$

And the inertia coefficients:

$$(I_1, I_1, I_2, I_3, I_4, I_5, I_6) = \int_{-h/2}^{h/2} \rho(z)(1, z, z^2 f(z), zf(z), [f(z)]^2)dz \tag{25}$$

The boundary conditions are described using edge displacements and forces as:

$$\begin{pmatrix} \text{at } x \text{ edges:} \\ either\ u\ or\ N_x \\ either\ v\ or\ N_{xy} \\ either\ w\ or\ M_{x,x} + 2M_{xy,x} \\ either\ w_{,x}\ or\ M_x \\ either\ \phi_x\ or\ P_x \\ either\ \phi_y\ or\ P_{xy} \end{pmatrix}, \quad \begin{pmatrix} \text{at } y \text{ edges:} \\ either\ v\ or\ N_{xy} \\ either\ u\ or\ N_{xy} \\ either\ w\ or\ M_{y,y} + 2M_{xy,x} \\ either\ w_{,y}\ or\ M_y \\ either\ \phi_x\ or\ P_{xy} \\ either\ \phi_y\ or\ P_y \end{pmatrix} \tag{26}$$

2.4 Navier's solution for rectangular plates with simply supports

The simply supported boundary conditions applied to the plate satisfy the following equations:

$$\begin{aligned} at\ x = 0, a: N_x = v = w = M_x = P_x = \phi_y = 0 \\ at\ y = 0, b: N_y = u = w = M_y = P_y = \phi_x = 0 \end{aligned} \tag{27}$$

However, non-classical boundary conditions controlled by:

$$\begin{aligned} at\ x = 0, a: \frac{\partial}{\partial x}\left(N_x, v, w, M_x, P_x, \phi_y\right) = 0 \\ at\ y = 0, b: \frac{\partial}{\partial y}\left(N_y, u, w, M_y, P_y, \phi_x\right) = 0 \end{aligned} \tag{28}$$

For the given boundary conditions, to solve Equation (24), the following Fourier series is used for the displacements:

$$\begin{aligned} u_0(x,t) &= \sum_m \sum_n U_{mn} \cos(\alpha x) \sin(\beta y)\, e^{i\omega_{mn} t} \\ v_0(x,t) &= \sum_m \sum_n V_{mn} \sin(\alpha x) \cos(\beta y)\, e^{i\omega_{mn} t} \\ w_0(x,t) &= \sum_m \sum_n W_{mn} \sin(\alpha x) \sin(\beta y)\, e^{i\omega_{mn} t} \\ \phi_x(x,t) &= \sum_m \sum_n \mathrm{X}_{mn} \cos(\alpha x) \sin(\beta y)\, e^{i\omega_{mn} t} \\ \phi_y(x,t) &= \sum_m \sum_n \mathrm{Y}_{mn} \sin(\alpha x) \cos(\beta y)\, e^{i\omega_{mn} t} \end{aligned} \tag{29}$$

where $\alpha = \left(\frac{m\pi}{a}\right), \beta = \left(\frac{n\pi}{b}\right)$, $i = \sqrt{-1}$, and ω_{mn} is the natural vibration frequency of the mode (m, n). U_{mn}, V_{mn} W_{mn}, X_{mn} and Y_{mn} are arbitrary coefficients. Substituting Equation (29) into Equation (23) the following eigenvalue equation is achieved.

$$(\mathrm{K} - \omega_{mn}^2 \mathrm{M})\mathrm{d} = 0 \tag{30}$$

Here, $\mathrm{d} = \{U_{mn} \quad V_{mn} \quad W_{mn} \quad X_{mn} \quad Y_{mn}\}^T$ are the vectors of the unknown coefficients. Additionally, K and M are the stiffness and mass matrices given in the Appendix Section with the coefficients. The following is used for the λ_{mn} dimensionless frequency parameter:

$$\lambda_{mn} = \omega_{mn}(a^2/h)\sqrt{\rho_m(1-v_m^2)/E_m} \tag{31}$$

3. RESULTS AND DISSUSSION

3.1 Validation

The proposed approach was validated by comparing the dimensionless frequencies of an FGM plate made of ZrO_2 / Ti-6Al-4V reviewed in Ref. (Huang and Shen, 2004). The dimensions of the square plates are assumed as $a = b = 0.2\,m$ and $h = 0.025\,m$ and with the material properties presented in Table 1. In the analyses, the dimensionless frequency parameter is specified by $\lambda_{mn} = \omega_{mn}(a^2/h)\sqrt{\rho_m(1-v_m^2)/E_m}, (T_0 = 300K)$ equation. The obtained results, presented in Table 2, imply that the findings of the current methodology are in good correlation with the analytical solution of (Huang and Shen, 2004). Where the properties are defined at $T_0 = 300K$, with $\rho_m = 4429\ kg/m^3, v_m = 0.3,\ E_m = 122.56\ GPa.$

Table 1. Temperature-dependent coefficients of the properties (Reddy and Chin 1998)

Material	*Property*	P_{-1}	P_0	P_1	P_2	P_3
Ti-6Al-4V	E (Pa)	0	122.56e9	-4.586e-4	0	0
	ρ (kg/m^3)	0	4512	0	0	0
	υ	0	0.2884	1.121e-4	0	0
	α (1K^{-1})	0	7.5788e-6	6.638e-4	-3.147e-6	0
	ψ (W/mK)	0	1	1.704e-4	0	0
ZrO_2	E (Pa)	0	244.27e9	-1.371e-3	1.214e-6	-3.681e-10
	ρ (kg/m^3)	0	5680	0	0	0
	υ	0	0.2882	1.133e-4	0	0
	α (1/K)	0	12.766e-6	-1.491e-3	1.006e-5	-6.778e-11
	ψ (W/mK)	0	1.700	1.276e-4	6.648e-8	0

Table 2. The frequency parameter $\lambda_{mn} = \omega_{mn}(a^2/h)\sqrt{\rho_m(1-v_m^2)/E_m}$ comparisons for ZrO_2/Ti-6Al-4V plate

	Huang. et al. (Huang and Shen, 2004)					Present HSDT				
Mode	(1,1)	(1,2)	(2,2)	(1,3)	(2,3)	(1,1)	(1,2)	(2,2)	(1,3)	(2,3)
p										
0.0	8.273	19.261	28.962	34.873	43.07	7.690	17.973	27.155	32.809	40.732
0.5	7.139	16.643	25.048	30.174	37.288	6.688	15.630	23.615	28.532	35.422
1	6.657	15.514	23.345	28.12	34.747	6.237	14.577	22.024	26.610	33.036
2	6.286	14.625	21.978	26.454	32.659	5.812	13.584	20.524	24.797	30.785
∞	5.4	12.571	18.903	22.762	28.111	5.042	11.784	17.764	21.463	26.646

3.2 Free Vibration Analyses

A small-scale simply supported square plate is treated for the free vibration behavior of the FGM nanoplate, with the sizes of a=1nm, b=a, and h=a/10. The plate assumed as made of ceramic (ZrO_2) and metal (Ti-6Al-4V) components based on the temperature-dependent material properties

provided in Table 2. The plate's frequencies ω_{mn} for the (m, n) modes are calculated using the eigenvalue Equation (31). Later the dimensionless frequency parameters are obtained with $\lambda_{mn} = \omega_{mn}(a^2/h)\sqrt{\rho_m(1-v_m^2)/E_m}$ equation. Here ρ_m, E_m, and v_m are the metal component's material properties at room temperature.

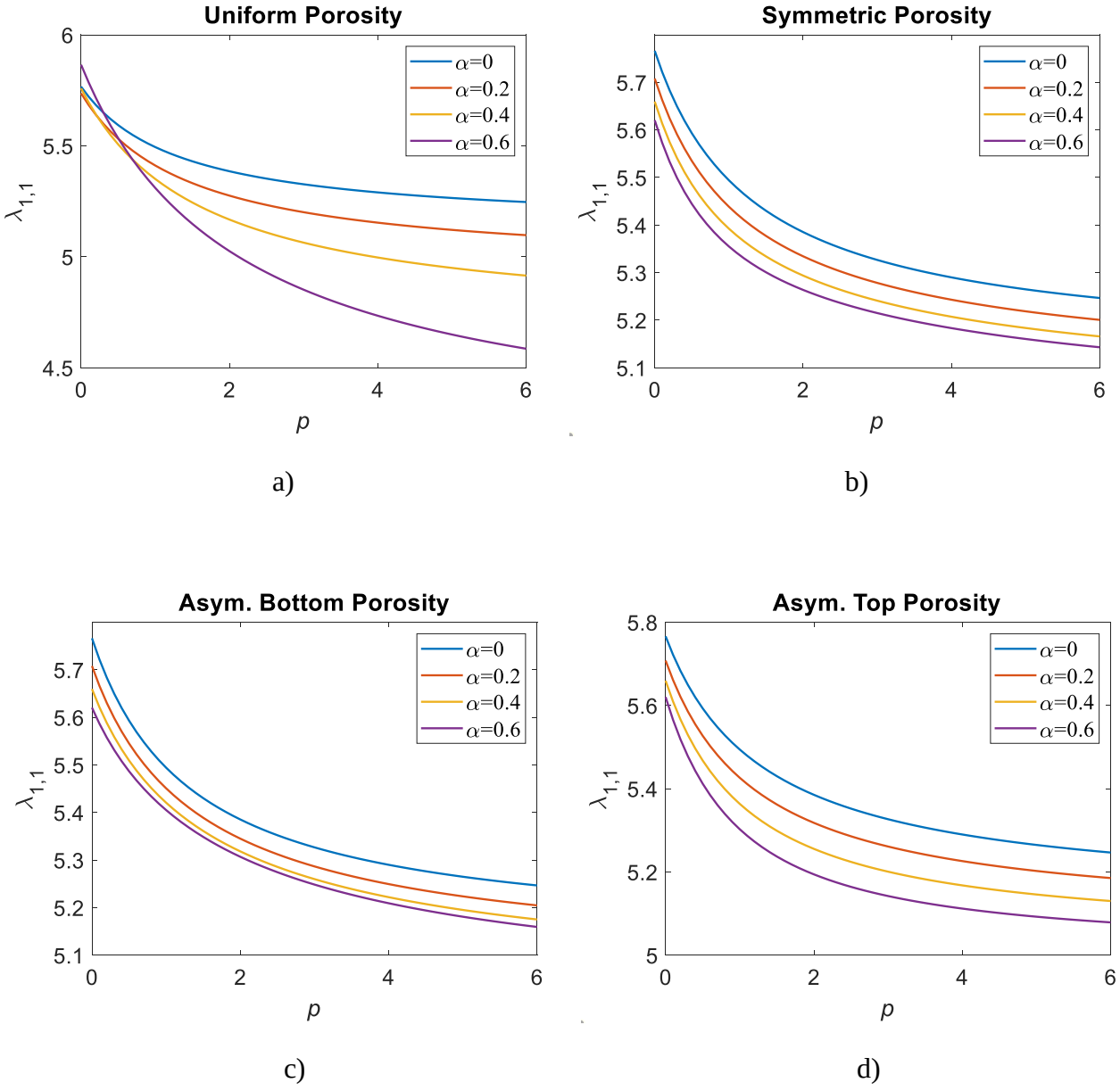

Figure 3. The dimensionless frequency $\lambda_{1,1}$ variation of nanoplate with different porosity patterns depending on the material grading constant (p=0.2-5) and porosity rate (α=0, 0.2, 0.4 and 0.6), for nonlocal e_0a=0 and material size l_m=0 parameters, and temperature rise ΔT=0

Considering the four porosity patterns, the $\lambda_{1,1}$ dimensionless frequency variations are depicted in Figure 3 depending on the material grading (power-law) constant p for the various porosity rates (α=0, 0.2, 0.4, and 0.6). Here, the temperature rise ΔT, and the nonlocal e_0a and material size l_m parameters are zero. As illustrated in Figure 3, the $\lambda_{1,1}$ dimensionless frequency of the nanoplate decays rapidly for $p \leq 2$. Afterwards, except for the uniform porosity α=0.6 case, the declining trend decelerates and approaches the limit for larger p values. This indicates that the nanoplate's metal

content is higher, and the entire composition tends towards a homogeneous metal structure. The main tendencies of the curves demonstrate that the dimensionless frequencies will drop as the stiffness of the plate is lowered for greater material grading constant values. However, as the porosity rate increases, the dimensionless frequency of the nanoplate also declines. Consequently, rising the porosity rate from 0 to 0.4 for the value of material grading constant p=2 reduced the calculated dimensionless frequency from 5.385 to 5.168, 5.294, 5.318, and 5.255 in uniform, symmetrical, asymmetrical bottom, and asymmetrical top porosity patterns, respectively. Accordingly, the influence of the porosity rate on the dimensionless frequency is in the order from the largest to the smallest as uniform, asymmetrical bottom, symmetrical, and asymmetrical top porosity patterns, respectively. Finally, as can be seen from Figure 3, due to the stiffness variation, both the porosity and its distribution function change the nanoplate's free vibration (Esen and Özmen, 2022a).

Figure 4a shows the frequency variation of the nanoplate with uniform porosity distribution depending on material grading constant and temperature rise for the constant value of porosity rate α=0.25 and e_0a=l_m=0. If the composition of the material is rich in ceramics, i.e., $p \leq 1$, the effect of the temperature increase is small due to the better temperature behavior of the ceramic in the composition. However, for all patterns, the increase in the metal component rapidly decreases the frequencies because of the softening influence of the temperature rise, as well as the lower strength compared to the ceramic-rich composition. In Figure 4b, the dimensionless frequency alterations of the nanoplate are presented for the different porosity patterns with the application of ΔT=50 K temperature rise. Accordingly, in each porosity pattern, the dimensionless frequency of the nanoplate decreased with the temperature rise. The effect of porosity patterns on dimensionless frequency in a ceramic-rich plate was also lower compared to a metal-rich plate. In other words, for a constant material grading constant, the dimensionless frequency differences between the porosity patterns increase as the metal ratio of the nanoplate is increased. Accordingly, in a nanoplate with a fully ceramic composition (p=0), the dimensionless frequency of the nanoplate decreased from 5.736 to 5.434 in uniform porosity, from 5.695 to 5.396 in symmetrical porosity, from 5.695 to 5.396 in asymmetric bottom porosity, and from 5.695 to 5.396 in asymmetric top porosity by increasing the temperature ΔT=50 K.

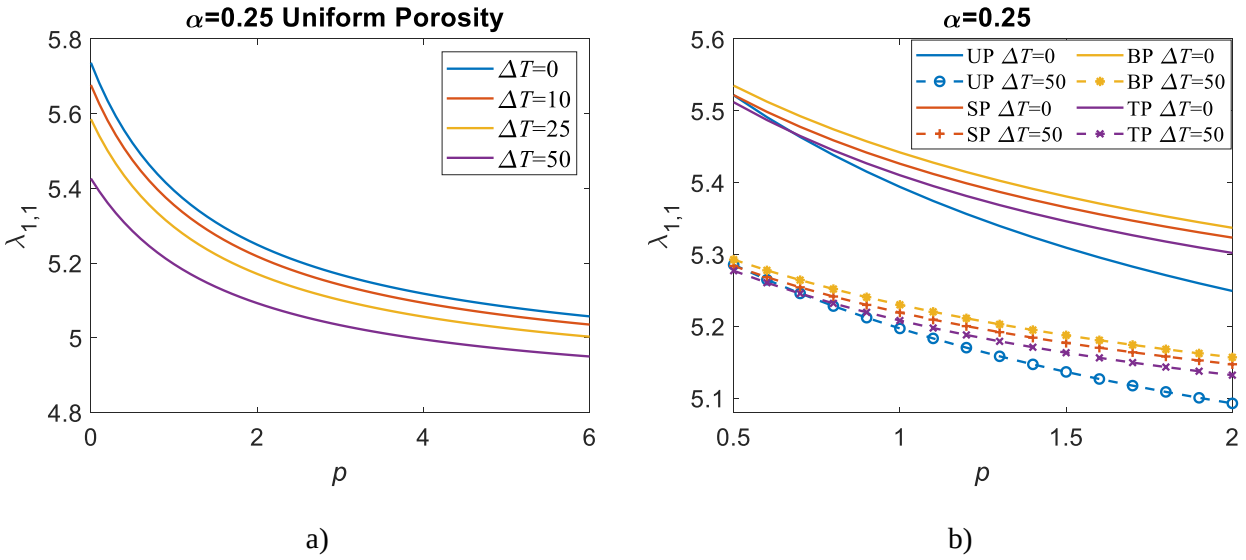

a) b)

Figure 4. a) The dimensionless frequency $\lambda_{1,1}$ variation of nanoplate with uniform porosity pattern dependent on the material grading constant (p=0-6) and temperature rise (ΔT=0, 10, 25 and 50 K) for porosity rate α=0.25, a/h=10, and e_0a =l_m =0. b)

Comparisons of uniform (UP), symmetric (SP), asymmetric bottom (BP), and asymmetric top (TP) porosity patterns dependent on the temperature rise ΔT=50 K

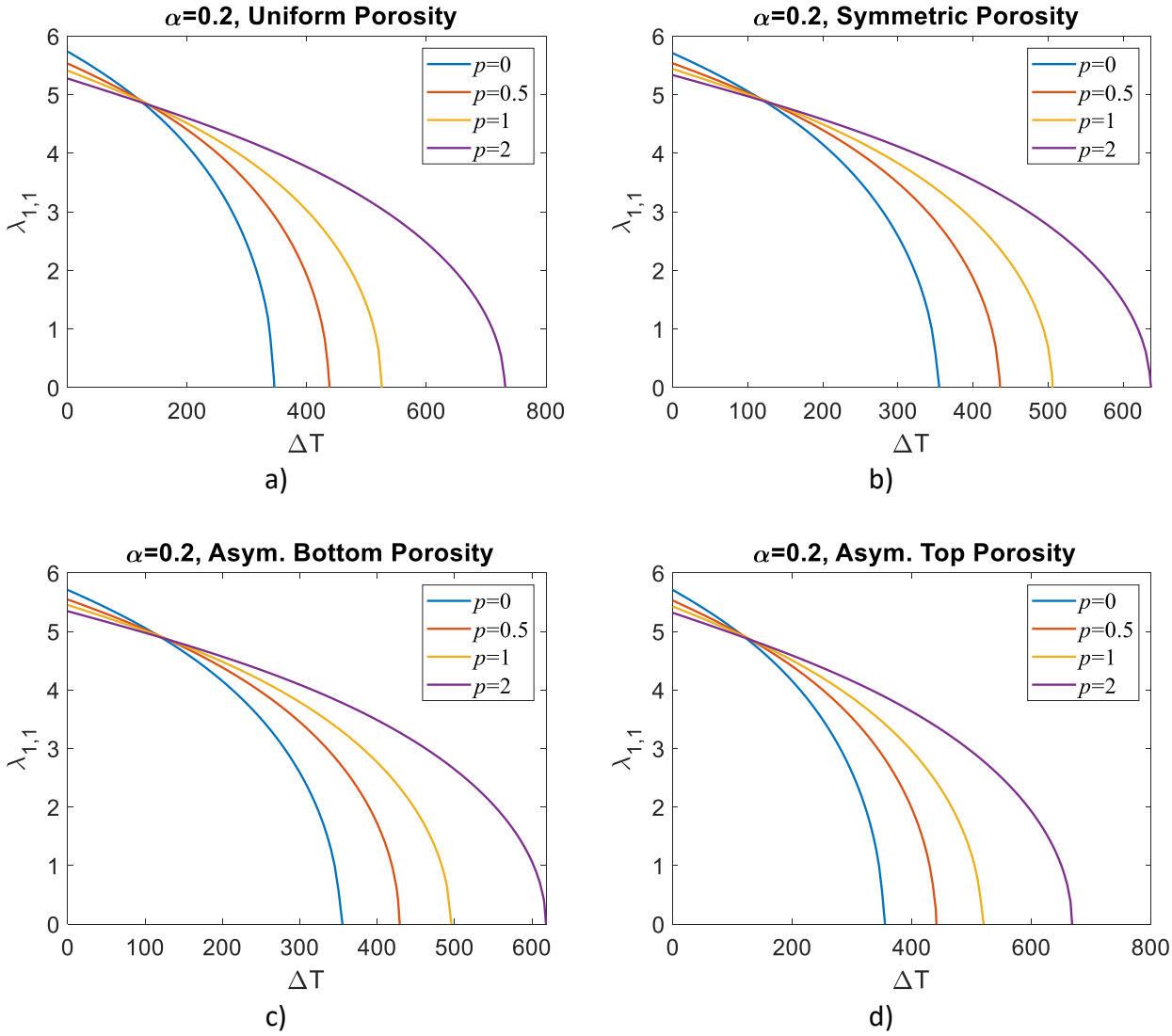

Figure 5. The dimensionless frequency $\lambda_{(1,1)}$ variations of of nanoplate with different porosity patterns dependent on the material grading constant (p=0, 0.5, 1, and 2) and temperature rise ΔT for porosity rate α=0.2, and a/h=10 and $e_0a=l_m=0$

Considering different porosity patterns, Figure 5 illustrates the impact of material grading constant on buckling temperatures for a porosity rate of α=0.2. In general, up to a temperature rise of approximately ΔT=120 K, increasing the material grading constant decreased the dimensionless frequencies in all porosity patterns. After the ΔT=120 K temperature rise, increasing the material grading constant slowed down the decrease rate of dimensionless frequency. According to the power law, at the value of material grading constant p=0, the plate is completely made of ZrO_2, and at p=2, approximately 83% of the plate is metal, and the remaining part is ZrO_2. Since the thermal expansion coefficient and density of Ti-6Al-4V (α_b=6.9414x10^{-6} 1/K and ρ_b= 4512 kg/m^3) at room temperature are lower than the thermal expansion coefficient and density of ZrO_2 (α_t=1.8590x10^{-5} 1/K and ρ_t= 5680 kg/m^3), the buckling temperature of the plate increased as the metal (Ti-6Al-4V) ratio in the plate increased. Therefore, as the metal composition in the nanoplate improved, the buckling temperature of the plate shifted towards higher temperature values. When comparing the porosity patterns, the buckling temperatures of the nanoplate at p=0 were calculated as 345.5 K, 355 K, 355 K, and 355.1 K in the uniform, symmetrical, asymmetrical bottom, and asymmetrical top porosity patterns, respectively. By

increasing the material grading constant to p=2, these temperature values, in turn, increased to 732 K, 637 K, 618 K, and 668.25 K in uniform, symmetrical, asymmetrical bottom, and asymmetrical top porosity patterns. Accordingly, the increase rates were obtained as 112%, 79.43%, 74.08%, and 88.23%, respectively.

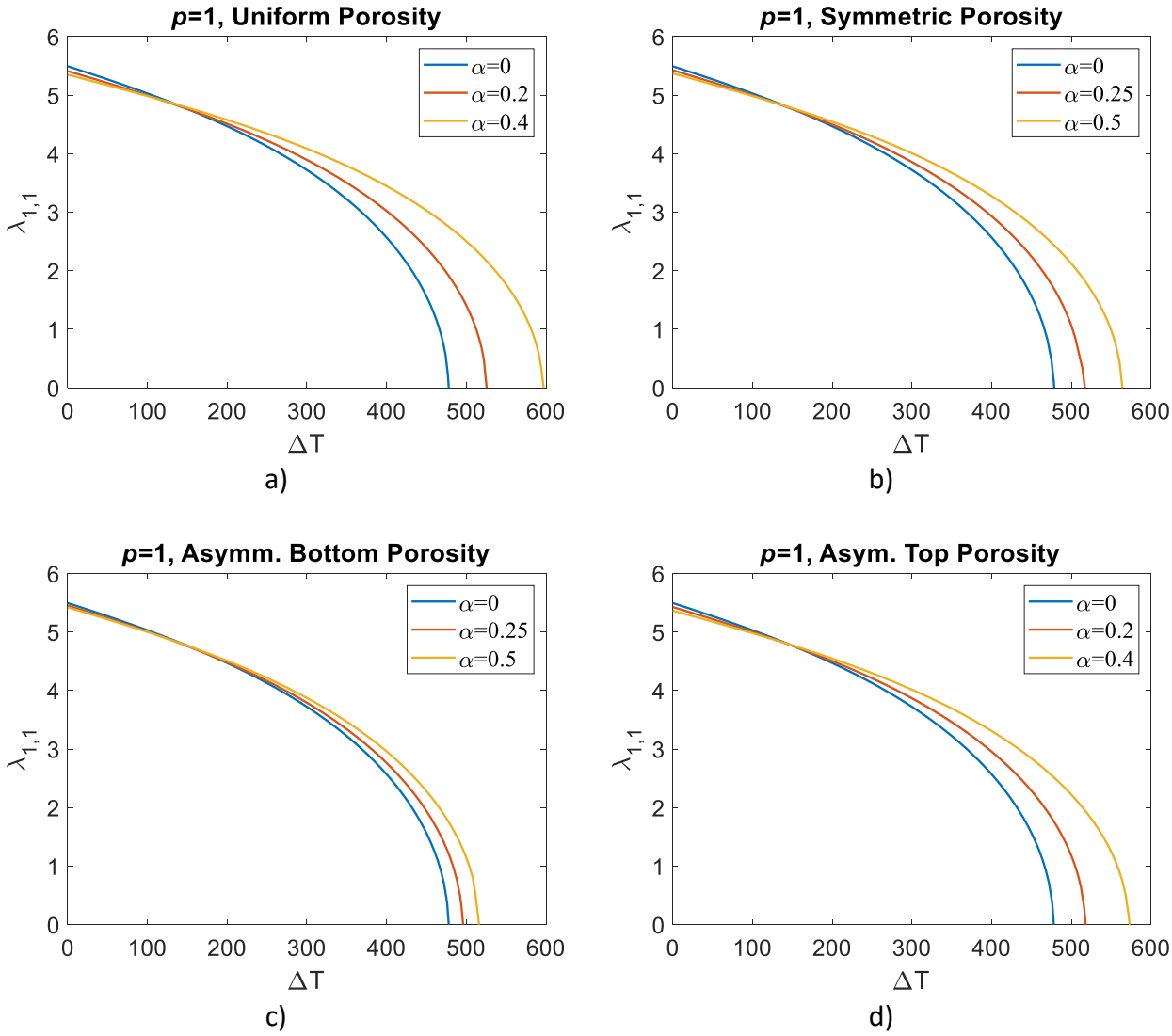

Figure 6. The dimensionless frequency $\lambda_{(1,1)}$ variations of nanoplate with different porosity patterns dependent on the porosity rate (α=0, 0.2, and 0.4) and temperature rise ΔT for porosity rate α=0.25, and a/h=10 and e_0a=l_m=0

Figure 6 displays the effect of porosity rate on buckling temperatures for four porosity patterns. In general, in all porosity patterns, the dimensionless frequencies decreased by increasing the porosity rate up to a temperature rise of approximately ΔT=140 K. However, increasing the porosity rate after ΔT=140 K temperature rise difference slowed down the decrease rate of dimensionless frequency. Therefore, the buckling temperatures of the nanoplate increased. When comparing the porosity patterns, the buckling temperatures of the nanoplate, which was computed as 478 K at α=0, increased to 597 K, 564 K, 516 K, and 573K in uniform, symmetrical, asymmetrical bottom, and asymmetrical top porosity patterns, respectively, by increasing the porosity rate of the nanoplate from 0 to 0.5. Accordingly, the increment rates were obtained as 24.89%, 17.99%, 7.94%, and 19.87%, respectively.

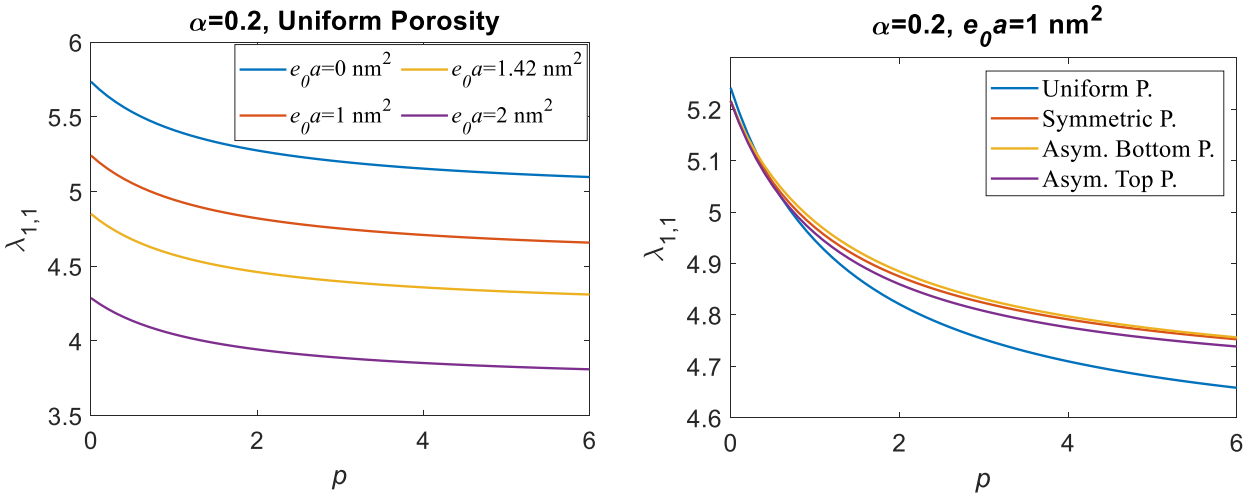

a) b)

Figure 7. a) The dimensionless frequency $\lambda_{(1,1)}$ variations of a nanoplate with uniform porosity distribution dependent on the material grading constant (p=0.2-5) and nonlocal parameter (e_0a=0, 1, 2 and 4 nm^2); for porosity rate α=0.2, and l_m=ΔT= 0. b) Comparisons of different porosity patterns for α=0.2, e_0a=1nm^2, and l_m=0.

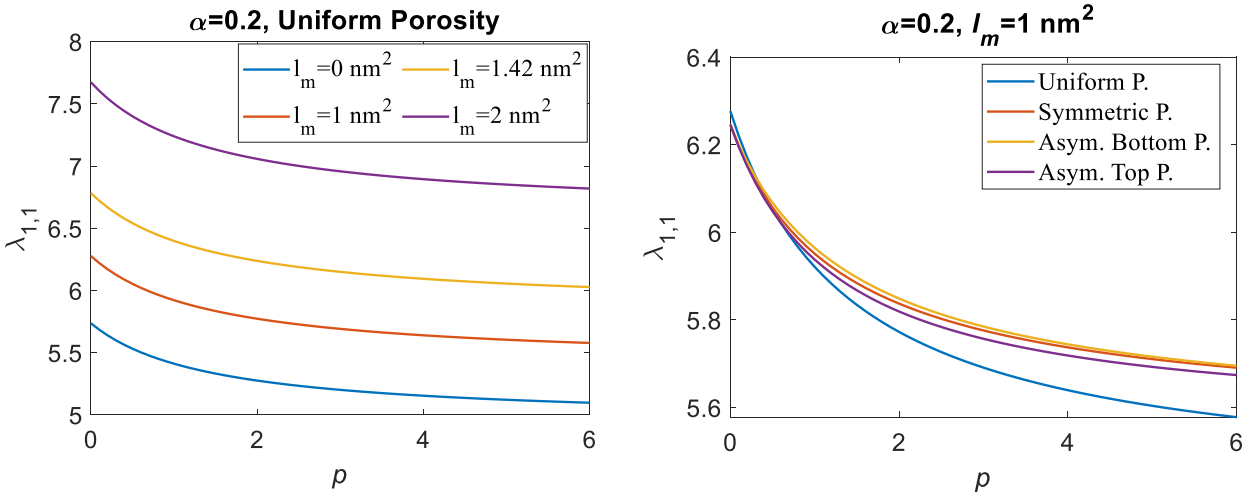

a) b)

Figure 8. a) The dimensionless frequency $\lambda_{1,1}$ variations of a nanoplate with uniform porosity distribution dependent on the material grading constant (p=0-6) and material size parameter (e_0a=0, 1, 2 and 4 nm^2); for porosity rate α=0.2, and l_m=ΔT= 0. b) Comparisons of different porosity patterns for α=0.2, e_0a=1nm^2, and l_m=0.

In case of uniform porosity distribution, Figure 7a shows the $\lambda_{1,1}$ frequency variation for several nonlocal parameters (e_0a=0, 1, 1.141 and 2 nm^2) and depending on the material grading constant (p=0-6). Figure 7b presents a comparison of the results of the porosity patterns for a constant nonlocal parameter value of e$_0$a=1 nm^2. In all analyses, the porosity rate is taken as α=0.2 and the temperature rise, and material size parameter are assumed to be zero. Due to the softening effect on the nanoplate (Eringen 1983; Talebizadehsardari et al. 2020; Esen and Özmen 2022b), the rise of the nonlocal parameter declines the frequencies inversely proportional to the size of the parameter. But the opposite results are witnessed in Fig 8, as a result of the material size parameter's stiffness-enhancing effect of the frequencies increase depending on its amount (Lim, Zhang, and Reddy 2015; Esen et al., 2021a). Here, for comparison, the amounts of nonlocal and dimensional parameters are considered the same in this study but may differ. The real values of these can be described by molecular dynamics simulations

(Giannopoulos et al., 2008) and experimental studies (Li and Hu, 2016). When an evaluation is made for the effects of porosity patterns for a fixed nonlocal and material size parameters, given in Figure 7b and Figure 8b, the dimensionless frequencies are obtained in the order of asymmetric bottom, symmetric, asymmetric top, and uniform porosity distribution patterns from higher to lower, respectively. As a result, while the nonlocal and material size parameters' stiffness-changing effects, in turn, caused only a decrease or increase in the dimensionless frequencies to a certain extent, the effect of the porosity patterns on the dimensionless frequencies did not change.

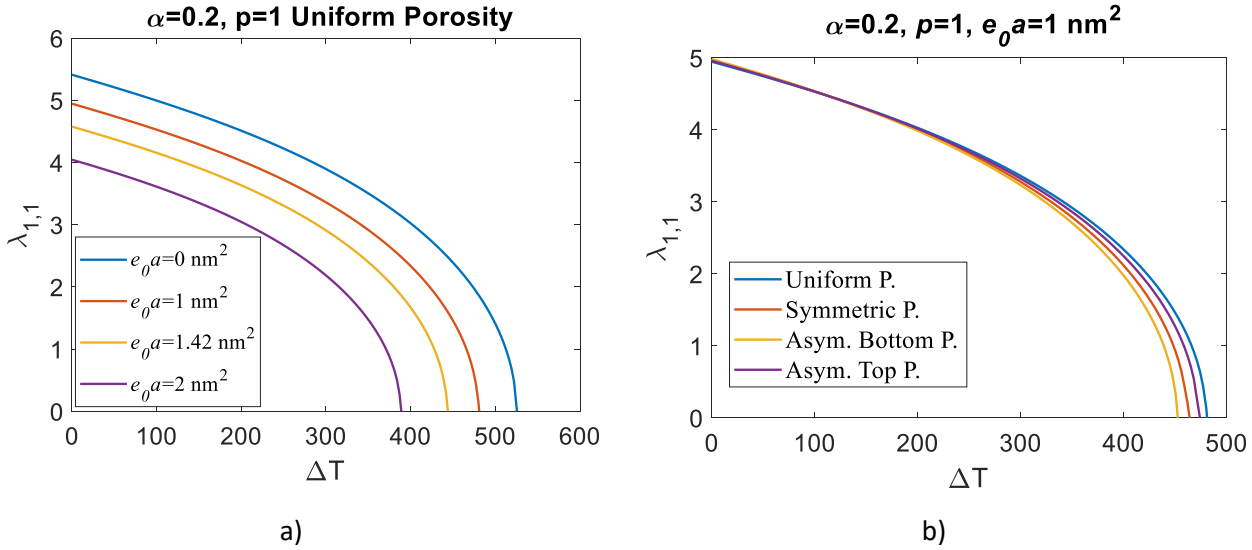

Figure 9. a) The dimensionless frequency $\lambda_{1,1}$ variations of a nanoplate with uniform porosity distribution depending on the nonlocal parameter (e_0a=0, 1, 2 and 4 nm^2) and temperature rise for porosity rate α=0.2 and l_m=0, b) Comparisons of different porosity patterns for α=0.2, p=1, e_0a=1nm^2, and l_m=0.

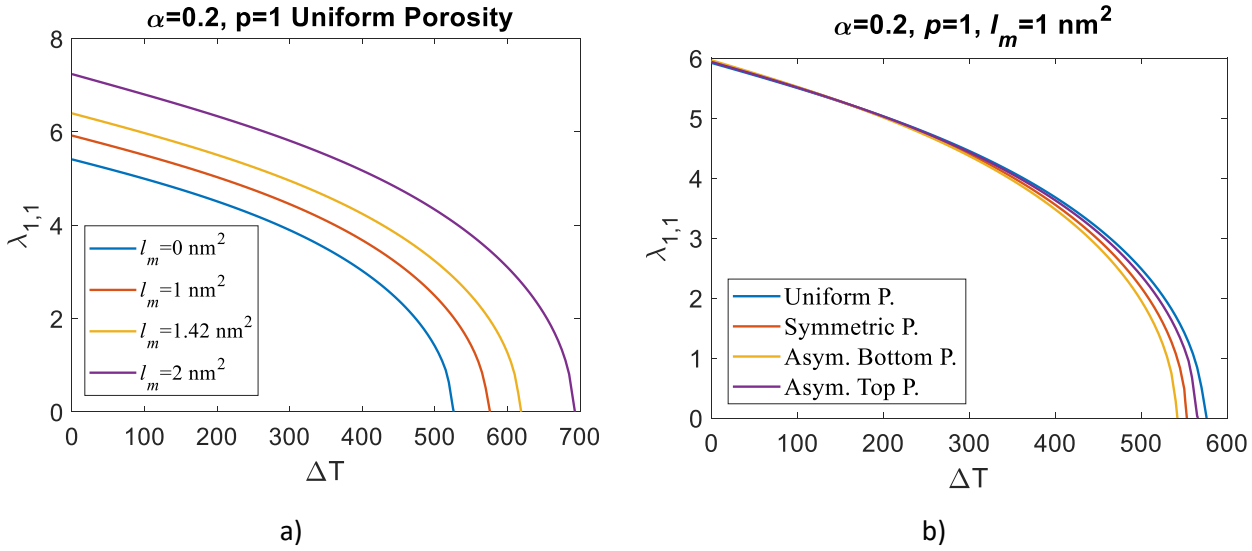

Figure 10. a) The dimensionless frequency $\lambda_{1,1}$ variations of a nanoplate with uniform porosity distribution depending on the material size parameter (l_m=0, 1, 2 and 4 nm^2), and temperature rise for porosity rate α=0.2 and e_0a=0, b) Comparisons of different porosity patterns for α=0.2, p=1, l_m =1nm^2, and e_0a =0.

In case of uniform porosity distribution, Figure 9a shows the frequency and buckling temperature variations depending on the several nonlocal parameter values (e_0a=0, 1, 1.141 and 2

nm^2) for a constant porosity rate (α=0.2) and material grading constant (p=1). Figure 9b presents a comparison of the porosity patterns for a constant nonlocal parameter value of e_0a=1 nm^2, α=0.2, and p=1. Due to the nonlocal parameter's softening effect on the nanoplate, the rise of this parameter decreases the dimensionless frequencies and buckling temperatures of the nanoplate reciprocally proportional to the size of the parameter (Esen and Özmen 2022a). But the opposite findings are observed in Figure 10a, because of the material size parameter's stiffness-enhancing effect, the frequencies and buckling temperatures increase depending on its amount. When an evaluation is made for the effects of porosity patterns for a fixed nonlocal and material size parameter, given in Figure 9. and Figure 10b, the buckling temperatures of the plate are obtained in the order of uniform, asymmetric top, symmetric, asymmetric bottom porosity distribution patterns from largest to smallest, respectively. In connection with this, buckling temperatures were calculated as 481 K, 474 K, 464 K, and 452.5 K in uniform, asymmetric top, symmetric, and asymmetric bottom porosity distribution patterns, with the inclusion of the nonlocal parameter, respectively. However, considering the material size parameter, these values were obtained as 576 K, 565 K, 553 K, and 542 K, respectively.

4. CONCLUSIONS

This study used the HSDT and NGST to pattern and analyze the free vibration behavior of an FGM porous nanoplate under thermal fields. Additionally, the effects of porosity distribution on the free vibration behavior of the plate are considered with four porosity patterns; uniform, symmetrical, asymmetric bottom, and up distribution patterns. Navier's method is employed for the solving of motion equations. Finally, the factors influencing the free vibration behavior of the porous FGM nanoplate are examined individually to get the results given below.

- The porosity and its distribution pattern alter the nanoplate's free vibration behavior. Additionally, the effect of porosity patterns on dimensionless frequency in a ceramic-rich plate is lower compared to a metal-rich plate.
- In all porosity patterns, the dimensionless frequencies decreased by increasing the porosity rate up to a temperature rise of approximately ΔT=140 K. After that, increasing the porosity rate slowed down the decrement rate of dimensionless frequency, thus increasing the buckling temperatures of the nanoplate. The buckling temperatures of the nanoplate, which was computed as 478 K at α=0, increased to 597 K, 564 K, 516 K, and 573K in uniform, symmetrical, asymmetrical bottom, and asymmetrical top porosity patterns, respectively, by increasing the porosity rate of the nanoplate from 0 to 0.5. Besides, rising the porosity rate from 0 to 0.4 for p=2 reduced the calculated dimensionless frequency from 5.385 to 5.168, 5.294, 5.318, and 5.255 in uniform, symmetrical, asymmetrical bottom, and asymmetrical top porosity patterns, respectively.
- The nanoplate's material content significantly influences the free vibration response and buckling temperatures.
- An increase in temperature softens the nanoplate, thus reducing its dimensionless frequencies.
- The nonlocal and material size parameters, in turn, cause the nanoplate to behave softer and stiffer depending on their size. Thus, the nonlocal parameter decreases the dimensionless frequencies and buckling temperatures while the material size parameter increases them. In this context, the buckling temperature was calculated as 481 K in a uniform porosity

distribution pattern, including the nonlocal parameter, respectively. However, this value was obtained as 576 K, including the material size parameter.

5. CONFLICT OF INTEREST

Authors approve that to the best of their knowledge, there is not any conflict of interest or common interest with an institution/organization or a person that may affect the review process of the paper.

6. AUTHOR CONTRIBUTION

Ramazan ÖZMEN contributed to determining the research and its management concept, data analysis and interpretation of the results, critical analysis of the intellectual content, manuscript preparation, and final approval and full responsibility.

7. REFERENCES

Aghababaei R., Reddy J.N., Nonlocal Third-Order Shear Deformation Plate Theory with Application to Bending and Vibration of Plates. Journal of Sound and Vibration, 326 (1–2), 277-289, 2009.

Akavci S.S., An Efficient Shear Deformation Theory for Free Vibration of Functionally Graded Thick Rectangular Plates on Elastic Foundation. Composite Structures 108 (1), 667–676, 2014.

Azeem P., B.M. R., Functionally Graded Materials (FGM) Fabrication and Its Potential Challenges & Applications. Materials Today: Proceedings (52) 413–418,2022.

Barati M.R., Zenkour A.M., Analysis of Postbuckling Behavior of General Higher-Order Functionally Graded Nanoplates with Geometrical Imperfection Considering Porosity Distributions. Mechanics of Advanced Materials and Structures 26 (12), 1081–88, 2019

Bendaho B., Belabed Z., Bourada M., Benatta M.A., Bourada F., Tounsi A., Assessment of New 2D and Quasi-3D Nonlocal Theories for Free Vibration Analysis of Size-Dependent Functionally Graded (FG) Nanoplates. Advances in Nano Research 7 (4), 277-292, 2019.

Biçer, H., Reactive Sintering of Boron Carbide Based Ceramics by SPS. Journal of Materials and Mechatronics:A (JournalMM), 3(1), 129-136, 2022.

Coskun S., Kim J., Toutanji H., Bending, Free Vibration, and Buckling Analysis of Functionally Graded Porous Micro-Plates Using a General Third-Order Plate Theory. Journal of Composites Science 3 (1), 15, 2019.

Doan T. L., Le P.B., Tran T.T., Trai V.K., Pham Q.H., Free Vibration Analysis of Functionally Graded Porous Nanoplates with Different Shapes Resting on Elastic Foundation. Journal of Applied and Computational Mechanics 7 (3), 1593-1605, 2021.

Eringen A.C., On Differential Equations of Nonlocal Elasticity and Solutions of Screw Dislocation and Surface Waves. Journal of Applied Physics 54 (9), 1983.

Eringen, A.C., Suhubi E.S., Nonlinear Theory of Simple Micro-Elastic Solids-I. International Journal of Engineering Science 2 (2), 189–203, 1964.

Esen I., Abdelrhmaan A.A., Eltaher M.A., Free Vibration and Buckling Stability of FG Nanobeams Exposed to Magnetic and Thermal Fields. Engineering with Computers, 38, 3463–3482, 2021a.

Esen I., Alazwari M.A., Eltaher M.A., Abdelrahman A.A., Dynamic Response of FG Porous Nanobeams Subjected Thermal and Magnetic Fields under Moving Load. Steel and Composite Structures 42 (6), 805-26, 2022.

Esen I., Daikh A.A., Eltaher M.A., Dynamic Response of Nonlocal Strain Gradient FG Nanobeam Reinforced by Carbon Nanotubes under Moving Point Load. The European Physical Journal Plus 136 (4), 458, 2021b.

Esen I., Dynamic Response of a Functionally Graded Timoshenko Beam on Two-Parameter Elastic Foundations Due to a Variable Velocity Moving Mass. International Journal of Mechanical Sciences Volumes (153–154), 21-35, 2019.

Esen I., Özarpa C., Eltaher M.A., Free Vibration of a Cracked FG Microbeam Embedded in an Elastic Matrix and Exposed to Magnetic Field in a Thermal Environment. Composite Structures (261),113552, 2021.

Esen I., Özmen R., Free and Forced Thermomechanical Vibration and Buckling Responses of Functionally Graded Magneto-Electro-Elastic Porous Nanoplates. Mechanics Based Design of Structures and Machines, 1–38, 2022b.

Esen I., Özmen R., Thermal Vibration and Buckling of Magneto-Electro-Elastic Functionally Graded Porous Nanoplates Using Nonlocal Strain Gradient Elasticity. Composite Structures (296) 115878, 2022a.

Giannopoulos G.I., Kakavas P.A., Anifantis N.K., Evaluation of the Effective Mechanical Properties of Single Walled Carbon Nanotubes Using a Spring Based Finite Element Approach. Computational Materials Science 41 (4), 561–69, 2008.

Huang X.L., Shen H.S., Nonlinear Vibration and Dynamic Response of Functionally Graded Plates in Thermal Environments. International Journal of Solids and Structures 41 (9–10), 2403-2427, 2004.

Jalaei M.H., Thai H.T., Dynamic Stability of Viscoelastic Porous FG Nanoplate under Longitudinal Magnetic Field via a Nonlocal Strain Gradient Quasi-3D Theory. Composites Part B: Engineering 175, 107164, 2019.

Ke L.L., Wang Y.S., Yang J., Kitipornchai S., Nonlinear Free Vibration of Size-Dependent Functionally Graded Microbeams. International Journal of Engineering Science 50 (1), 256-267, 2012.

Kiani Y., Thermal Post-Buckling of FG-CNT Reinforced Composite Plates. Composite Structures 159, 299-306, 2017.

Kong S., Zhou S., Nie Z., Wang K., The Size-Dependent Natural Frequency of Bernoulli-Euler Micro-Beams. International Journal of Engineering Science 46 (5), 427-447, 2008.

Li L., Hu Y., Buckling Analysis of Size-Dependent Nonlinear Beams Based on a Nonlocal Strain Gradient Theory. International Journal of Engineering Science (97) 84–94, 2015.

Li L., Hu Y., Nonlinear Bending and Free Vibration Analyses of Nonlocal Strain Gradient Beams Made of Functionally Graded Material. International Journal of Engineering Science (107), 77-99, 2016.

Lim C.W., Zhang G., Reddy J.N., A Higher-Order Nonlocal Elasticity and Strain Gradient Theory and Its Applications in Wave Propagation. Journal of the Mechanics and Physics of Solids (78), 298-313, 2015.

Najafi F., Shojaeefard M.H., Googarchin H.S., Nonlinear Dynamic Response of FGM Beams with Winkler–Pasternak Foundation Subject to Noncentral Low Velocity Impact in Thermal Field. Composite Structures (167) 132-43, 2017.

Reddy J.N., Chin C.D., Thermomechanical Analysis of Functionally Graded Cylinders and Plates. Journal of Thermal Stresses 21 (6) 593–626, 1998.

Reddy J.N., Nonlocal Theories for Bending, Buckling and Vibration of Beams. International Journal of Engineering Science 45 (2–8), 288-307, 2007.

Reddy JN.,A Simple Higher-Order Theory for Laminated Composite Plates. Journal of Applied Mechanics 51 (4), 745–752, 1984.

Şanlı, P., Gavas, M., Microstructure, Physical and Mechanical Properties of Al/SiC and Al/B4C Metal Matrix Composites Produced by Powder Metallurgy. Journal of Materials and Mechatronics: A (JournalMM), 2(2), 72-89, 2021.

Talebizadehsardari P., Salehipour H., Shahgholian-Ghahfarokhi D., Shahsavar A., Karimi M., Free Vibration Analysis of the Macro-Micro-Nano Plates and Shells Made of a Material with Functionally Graded Porosity: A Closed-Form Solution." Mechanics Based Design of Structures and Machines 0 (0), 1-27, 2020.

Touloukian Y.S., Thermophysical Properties of High Temperature Solid Materials. Macmillan New York, 1967

Zenkour A.M., A Comprehensive Analysis of Functionally Graded Sandwich Plates: Part 1-Deflection and Stresses. International Journal of Solids and Structures 42 (18-19) 5224–42, 2005.

Zenkour A.M., Alghamdi N.A., Bending Analysis of Functionally Graded Sandwich Plates Under the Effect of Mechanical and Thermal Loads. Mechanics of Advanced Materials and Structures 17 (6) 419-32, 2010.

Zhang C., Ji H., Xu H., Liang M., Huang J., Pei S., Li M., Interfacial Microstructure and Mechanical Properties of Ultrasonic-Assisted Brazing Joints between Ti–6Al–4V and ZrO_2. Ceramics International 46 (6) 7733–7740, 2020.

Zhang X., Zhang G., Li J., He X., Wang Y., Hang R., Huang X., Tang B., Chu P.K., Cellular Response to Nano-Structured Zr and ZrO_2 Alloyed Layers on Ti-6Al-4V. Materials Science and Engineering (90) 523-530, 2018.

Zhou X., Zhang M., Xu D., Geng S., Wang Q., Wang F., Microstructural Evolution, Corrosion Behavior and Cytotoxicity of Ti-6Al-4V/ZrO_2 Composite Fabricated by Directed Energy Deposition for Implant Biomaterial." Journal of Alloys and Compounds (892) 161820, 2022.

8. APPENDIX

$$\mathrm{K}_{11} = (A_{11}\alpha^2 + A_{66}\beta^2)c_2 \qquad \mathrm{K}_{12} = (A_{12} + A_{66})\beta\alpha c_2$$

$$\mathrm{K}_{13} = -B_{11}\alpha^3 c_2 \qquad \mathrm{K}_{14} = (C_{11}\alpha^2 + C_{66}\beta^2)c_2$$

$$\mathrm{K}_{15} = (C_{12} + C_{66})\beta\alpha c_2 \qquad \mathrm{K}_{21} = \mathrm{K}_{12}$$

$$\mathrm{K}_{22} = (A_{66}\alpha^2 + A_{22}\beta^2)c_2 \qquad \mathrm{K}_{23} = -B_{22}\alpha^3 c_2$$

$$\mathrm{K}_{24} = \mathrm{K}_{15} \qquad \mathrm{K}_{25} = (C_{66}\alpha^2 + C_{22}\beta^2)c_2$$

$$\mathrm{K}_{31} = \mathrm{K}_{13} \qquad \mathrm{K}_{32} = \mathrm{K}_{23}$$

$$\mathrm{K}_{33} = (D_{11}\alpha^4 + 2D_{12}\alpha^2\,\beta^2 + 4D_{66}\alpha^2\,\beta^2 + D_{22}\beta^4)c_2 + \left(-N_{xx}^T\alpha^2 - N_{yy}^T\beta^2\right)c_1 \quad \text{A1}$$

$$\mathrm{K}_{34} = -(E_{11}\alpha^3 + (E_{12} + 2E_{66})\alpha\beta^2)c_2 \qquad \mathrm{K}_{43} = \mathrm{K}_{34}$$

$$\mathrm{K}_{35} = -(E_{22}\beta^3 + (E_{12} + 2E_{66})\alpha^2\beta)c_2 \qquad \mathrm{K}_{53} = \mathrm{K}_{35}$$

$$\mathrm{K}_{44} = (F_{55} + G_{11}\alpha^2 + G_{66}\beta^2\,)c_2 \qquad \mathrm{K}_{41} = \mathrm{K}_{14}$$

$$\mathrm{K}_{45} = (G_{12} + G_{66}\,)\alpha\beta c_2 \qquad \mathrm{K}_{42} = \mathrm{K}_{24}$$

$$\mathrm{K}_{51} = \mathrm{K}_{15} \qquad \mathrm{K}_{52} = \mathrm{K}_{25}$$

$$\mathrm{K}_{53} = \mathrm{K}_{35} \qquad \mathrm{K}_{54} = \mathrm{K}_{45}$$

$$\mathrm{K}_{55} = (F_{44} + G_{66}\alpha^2 + G_{22}\beta^2\,)c_2$$

$$\mathrm{M}_{11} = I_1 c_1 \quad \mathrm{M}_{12} = 0 \quad \mathrm{M}_{13} = -\alpha I_2 c_1 \quad \mathrm{M}_{14} = I_4 c_1 \quad \mathrm{M}_{15} = 0$$

$$\mathrm{M}_{21} = 0 \quad \mathrm{M}_{22} = I_1 c_1 \quad \mathrm{M}_{23} = -\beta I_2 c_1 \quad \mathrm{M}_{24} = 0 \quad \mathrm{M}_{25} = I_4 c_1$$

$$\mathrm{M}_{31} = -\alpha I_2 c_1 \quad \mathrm{M}_{32} = -\beta I_2 c_1 \quad \mathrm{M}_{33} = I_3(\alpha^2 + \beta^2)c_1 + I_1 c_1 \quad \mathrm{M}_{34} = -\alpha I_5 c_1 \quad \mathrm{M}_{35} = -\beta I_5 c_1 \quad \text{A2}$$

$$\mathrm{M}_{41} = \mathrm{M}_{14} \quad \mathrm{M}_{42} = 0 \quad \mathrm{M}_{43} = -\alpha I_5 c_1 \quad \mathrm{M}_{44} = I_6 c_1 \quad \mathrm{M}_{45} = 0$$

$$\mathrm{M}_{51} = 0 \quad \mathrm{M}_{52} = I_4 c_1 \quad \mathrm{M}_{53} = -\beta I_5 c_1 \quad \mathrm{M}_{54} = 0 \quad \mathrm{M}_{55} = I_6 c_1$$

$$c_1 = 1 + (ea)^2(\alpha^2 + \beta^2) \qquad c_2 = 1 + l_m^2(\alpha^2 + \beta^2)$$